

# Morphology around Nanopores Fabricated by Laser-Assisted Dielectric Breakdown and Its Impact on Ion and DNA Transport and Sensing

Ming Dong, Reza Nouri, Zifan Tang, and Weihua Guan\*



Cite This: *ACS Appl. Mater. Interfaces* 2023, 15, 24747–24755



Read Online

ACCESS |



Metrics & More



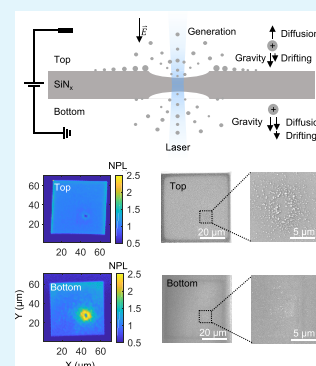
Article Recommendations



Supporting Information

**ABSTRACT:** Laser-assisted controlled dielectric breakdown (LaCBD) has emerged as an alternative to conventional CBD-based nanopore fabrication due to its localization capability, facilitated by the photothermal-induced thinning down in the hot spot. Here, we reported the potential impact of the laser on forming debris around the nanopore region in LaCBD. The debris was clearly observable by scanning electron microscopy (SEM) and photoluminescence (PL) spectroscopy. We found that debris formation is a unique phenomenon in LaCBD that is not observable in the conventional CBD approach. We also found that the LaCBD-induced debris is more evident when the laser power and voltage stress are higher. Moreover, the debris is asymmetrically distributed on the top and bottom sides of the membrane. We also found unexpected rectified ionic and molecular transport in those LaCBD nanopores with debris. Based on these observations, we developed and validated a model describing the debris formation kinetics in LaCBD by considering the generation, diffusion, drift, and gravity in viscous mediums. These findings indicate that while laser aids in nanopore localization, precautions should be taken due to the potential formation of debris and rectification of molecular transport. This study provides valuable insights into the kinetics of LaCBD and the characteristics of the LaCBD nanopore.

**KEYWORDS:** nanopore, laser-assisted dielectric breakdown, photoluminescence, morphology, rectification



## 1. INTRODUCTION

The traditional transmission electron microscope (TEM) drilling and controlled breakdown (CBD) for  $\text{SiN}_x$  nanopore fabrication were limited in cost and reliability.<sup>1–4</sup> The TEM method needs a costly platform and requires trained professionals.<sup>1,2,5</sup> Although the CBD approach was proposed as an attractive low-cost, highly accessible alternative, there are numerous reliability issues in controlling and determining the number and location of the formed nanopore.<sup>6,7</sup> To address these issues, laser-assisted dielectric breakdown (LaCBD) was developed as a cost-effective and reliable method for localized single nanopore fabrication.<sup>8</sup> The mechanism of this method is based on the photothermal etching effect caused by the focused laser beam and the dielectric breakdown induced by the electric field.<sup>8,9</sup> This method can form a single nanopore at the laser's focused position.

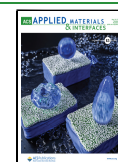
While LaCBD was proposed as a cost-effective method for localized single nanopore fabrication, there is still a lack of comprehensive research on the laser etching mechanism, pore region morphology, and molecular transport behavior. To explore the laser etching mechanism, Yamazaki et al. showed that the  $\text{SiN}_x$  etching rate was influenced by the supporting electrolyte concentration and suggested that the photothermal effect was responsible for the  $\text{SiN}_x$  dissolution process.<sup>8</sup> Gilboa et al. showed that Si-rich  $\text{SiN}_x$  membranes would have faster etching rates and be further accelerated in an alkaline

environment.<sup>10</sup> They hypothesized that hydroxyl ion is a catalyst for the hydrolysis that promotes the dissolution of  $\text{SiN}_x$ , and the increased etching speed under high pH verifies the hypothesis. However, the detailed dynamics of the  $\text{SiN}_x$  dissolution process and the actual laser etching mechanism remain unclear. The liquid phase environment in LaCBD gives the etched material a chance to be deposited on the membrane. Previous works found that materials may have resolidification around the pore region during laser etching.<sup>11,12</sup> Regarding the pore region morphology, previous works used TEM/AFM to characterize the pore region on the single side of the  $\text{SiN}_x$  membrane, and they proved the Gaussian thickness profile of the etching spot.<sup>8,13</sup> However, broader morphology characterization of both sides is needed to understand the kinetics in LaCBD. Besides the pore region morphology, few works studied the molecular transport behavior in the LaCBD nanopore. When applying the LaCBD nanopore for molecular detection, previous works showed that the molecular transport

Received: March 3, 2023

Accepted: April 26, 2023

Published: May 10, 2023



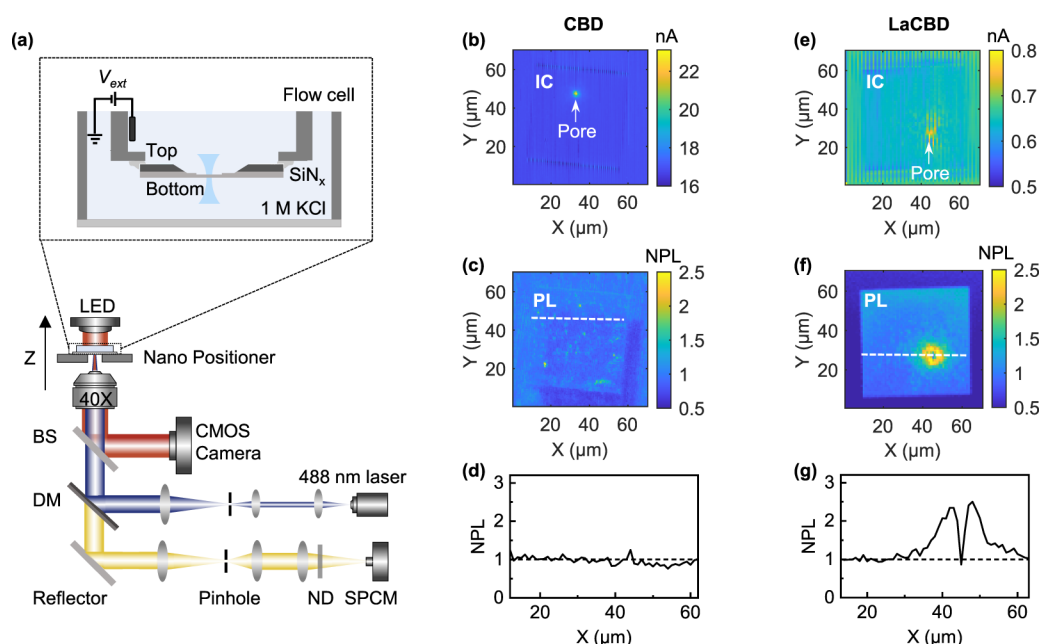


**Figure 1.** (a) Schematics of the LaCBD setup. The ionic current map (b), PL map (c), and PL line profile (d) across the pore region of a traditional CBD nanopore (using +18 V voltage stress). The ionic current map (e), PL map (f), and PL line profile (g) across the pore region of a LaCBD nanopore (using 20 mW laser and +3 V voltage stress). NPL is the normalized PL intensity over the intact membrane region.

is directionally dependent, and they found different capture rates for DNA entering from either side.<sup>8</sup> Based on the rectified DNA transport, the pore shape was hypothesized to be asymmetric and funnel-like. However, direct geometry evidence is needed to prove that the pore has a asymmetric shape. To enhance our understanding of the characteristics of the LaCBD nanopore, it is necessary to conduct further studies on the laser etching dynamics and pore region morphology.

In this work, we reported the potential impact of the laser on debris formation around the nanopore region in LaCBD. This unique phenomenon is not observable in the conventional CBD method. The SEM and photoluminescence (PL) spectroscopy characterization confirmed the presence of debris, which was asymmetrically distributed on the top and bottom sides of the membrane. An unexpected rectified ionic and molecular transport was also found in those LaCBD nanopores with debris. Based on these observations, we developed and validated a model describing the debris formation kinetics in LaCBD by considering the generation, diffusion, drift, and gravity in viscous mediums. The model and experimental results suggested that higher laser power or voltage stress would escalate debris formation in LaCBD. These findings suggest that while the laser helps localize nanopores in LaCBD, caution should be taken due to the possibility of debris formation and rectification of molecular transport. This study would provide valuable insights into the kinetics of LaCBD and the characteristics of the LaCBD nanopore.

## 2. RESULTS AND DISCUSSION

**2.1. Abnormal PL Profile around the Nanopore Observed in LaCBD.** We used a previously reported platform to fabricate CBD and LaCBD nanopores (shown in Figure 1a, see Methods for setup details).<sup>9</sup> With this setup, we can perform the nanopore fabrication and characterizations in situ, including monitoring the conductance (IV), PL mapping for microscopic material variations, and laser-enhanced ionic

current mapping for locating the nanopores. The LaCBD method is based on the photothermal etching effect caused by the focused laser beam and the dielectric breakdown induced by the electric field. The previous study shows that the peak temperature at the laser's focal point decreases rapidly to room temperature when away from the focal point.<sup>8,9</sup> Besides, photothermal etching can accelerate as temperature increases.<sup>8</sup> Therefore, to ensure repeatable and fast etching, we develop an auto-focusing method to focus the laser tightly on the SiNx membrane (see Methods and Figure S1 for details of auto-focusing and current traces for breakdown).

Before and after nanopore fabrication, the SiNx membrane is examined by laser-enhanced ionic current (IC) mapping and PL mapping. The IC mapping (Figure 1b,e) is used to locate the fabricated nanopore's position, and PL mapping (Figure 1c,f) is a well-established technique to probe the material's microscopic structures.<sup>9,14</sup> In the PL characterization, the variations in PL intensity may result from three microscopic factors: changes in electronic structure, SiNx membrane thickness, and surface roughness.<sup>14,15</sup> For the traditional CBD approach, the nanopore is formed by accumulating defects in the membrane. Considering the nanometer scale of the channel, the material removal should be minimal. The PL characterization (Figure 1c,d) suggests that the CBD will not induce noticeable PL change. Compared to the CBD, as previously reported, the LaCBD method should reduce the PL intensity at the pore region due to the micrometer scale material removal.<sup>7,8,10,16</sup> In addition, the laser beam can modify electronic structures even without membrane thinning, decreasing PL.<sup>14</sup> Thus, the PL of the LaCBD nanopore region should typically decrease due to the removal of material and the altered electronic structure. However, our experiments observed an unexpected donut-shaped PL increment around the LaCBD pore (Figure 1f). The line profile (Figure 1g) across the pore region indicates that the PL intensity increased more than two times compared to the intact membrane region. This PL increment indicates that either the electronic structure

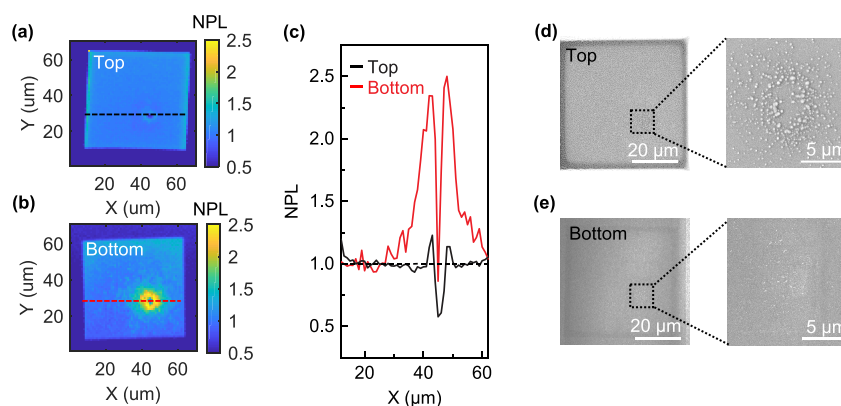


**Figure 2.** (a) Top-side PL map. (b) Bottom-side PL map. (c) PL line profile across the pore region of the top side and bottom side. (d) Top-side SEM image. (e) Bottom-side SEM image. Insets are enlarged views of SEM images. The SEM characterization shows different morphology patterns between the top and bottom surfaces.

is changed or the thickness is increased around the pore region.<sup>14,15</sup> This unique phenomenon is repeatedly observed in the experiments (Figure S2a shows three additional samples with PL increment). Besides, this PL increment phenomenon is also observed in the 12 nm-thick SiN<sub>x</sub> samples (Figure S3). Since the previous study suggests that a combination of high laser power and the low electric field is statistically favorable for forming a single nanopore at a designated location,<sup>9</sup> a 20 mW laser and a voltage stress less than +6 V (0.2 V/nm) are used in most nanopores' fabrication. While high laser power and low electric field are preferred in LaCBD nanopore fabrication, it also has an abnormal PL increment around the pore. Thus, the microscopic structures of the pore region need to be characterized to help understand the mechanism of LaCBD and the origination of the abnormal PL increment.

**2.2. PL Increment Due to Excess Debris around the Pore.** To further inspect the microscopic structures of the LaCBD nanopore with abnormal PL increment, the SiN<sub>x</sub> membrane in Figure 1f was flipped and re-mapped with the laser to get its top-side PL map (Figure 2a). Interestingly, although both sides show PL increment around the pore (Figure 2a,b), the increment amplitude showed an asymmetrical pattern for two sides (Figure 2c): the bottom side has a higher PL increment (~2.25 times) around the pore than the top side (~1.25 times). The actual morphology around the pore is of great interest since the asymmetrical PL profile may arise from multiple factors. Through SEM characterization (Figure 2d,e), we found excess debris around the pore on the top surface and those particles' diameters ranged from 50 to 200 nm. Another sample's SEM images show a similar pattern in Figure S2b. Previous works indicated that thinned membranes and altered electronic structures would cause PL to decrease.<sup>7,8,14</sup> Thus, the observed debris should be the main contributing factor to PL increment. Besides, the donut-shaped distribution of debris fits well with the increased PL pattern, which further indicates that excess debris should be the primary origin of the PL increment. Interestingly, the distribution of debris also showed an asymmetrical profile for each side: the top side has much more particles than the bottom side (Figure 2d,e, Figure S2b). However, the asymmetrical morphology profile (the top side has more debris) looks contradictory to the PL profile (the top side has a lower PL increment). The laser penetration depth and surface roughness can explain this counterintuitive result. The penetration depth (>100 nm) of the 488 nm laser is more

than the thickness of the SiN<sub>x</sub> membrane (30 nm).<sup>17</sup> Therefore, the debris on both sides can contribute to the increment of PL intensity, no matter mapping on the bottom or top surfaces. The PL map of both sides should have a similar intensity due to the deep penetration depth. However, the different surface roughness can reduce the PL intensity by scattering photons.<sup>15</sup> Based on the SEM images, the pore region on the top side has a higher degree of roughness than the bottom. This higher roughness can scatter away photons and result in lower PL intensity when mapping on the top surface. In observing this correlation between debris and PL intensity, it is preferable to use PL mapping on the bottom surface since it has a higher signal-to-noise ratio to indicate the excess debris around the pore.

Compared to SEM characterization, PL mapping can be a convenient in situ tool for indicating the excess material on both sides (higher PL increment means more debris deposited). Although clear evidence from SEM images shows debris existing around the LaCBD nanopore, the kinetics of debris formation are yet to be discovered. This phenomenon of debris formation around nanopores was not observed in traditional CBD and TEM methods.<sup>6,18</sup> The LaCBD method, which involves laser drilling and voltage-induced breakdown in the salt solution, is more complex compared to traditional CBD and TEM methods. Therefore, the more complicated etching mechanism and material migration in the LaCBD environment need further exploration to explain the debris formation.

**2.3. Model for Debris Formation and Validation via PL Characterization.** We hypothesized that debris formation around the LaCBD nanopore results from the competition between material decomposition and deposition in the LaCBD fabrication. Previous works showed that during LaCBD, the chloride (Cl<sup>-</sup>) and hydroxide (OH<sup>-</sup>) ions can promote the oxidation and etching of SiN<sub>x</sub>.<sup>7,8,10</sup> Another work also shows that the etching process can be understood as a reaction pathway that allows for a self-accelerating dissolution process of silica, namely, hydrolysis with hydroxide ions.<sup>19</sup> The hydrolysis of silica will produce silicic acid, which mainly exists as a positively charged specie. The evidence from these works shows that the laser-induced SiN<sub>x</sub> etching can be explained through three steps. First, the chloride ions will replace Si-Si bonds on the SiN<sub>x</sub> surface. Second, the hydroxide ions will replace the chloride ions and form silica.



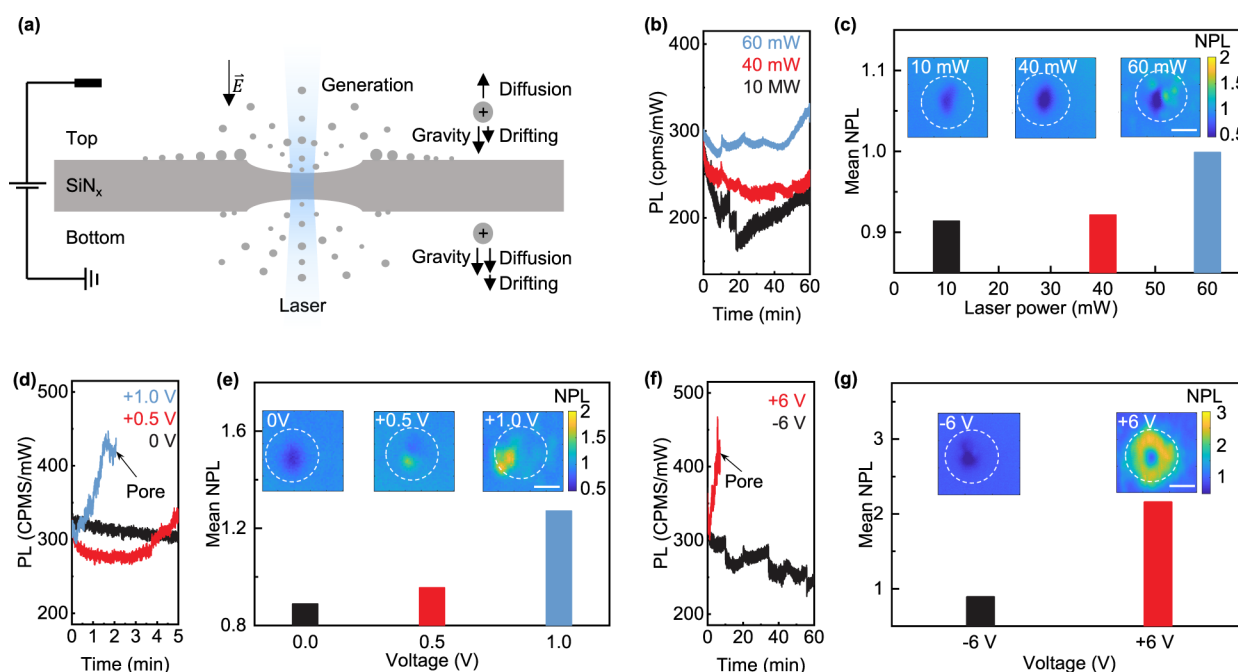


**Figure 3.** (a) Schematic of debris deposition on the top and bottom surfaces induced by a combination effect of generation, diffusion, drifting, and gravity. (b) Real-time PL intensity during laser etching. 10, 40, and 60 mW lasers were used, and no voltage was applied. (c) PL mapping of the etched region and the mean PL inside the white dashed circle. (d) Real-time PL intensity during laser etching. 0, +0.5, and +1.0 V voltage were used, and 20 mW lasers were applied. (e) PL mapping of the etched region and the mean PL inside the white dashed circle. (f) Real-time PL intensity during laser etching. +6 and -6 V voltages were used, and 20 mW lasers were applied. (g) PL mapping of the etched region and the mean PL inside the white dashed circle. The scale bar is 5  $\mu\text{m}$ .

Third, silica's self-accelerating and heat-promoted dissolution will generate positively charged silicic acid ions.

Since the dissolved silicic acid ion is positively charged, its movement will be affected by the electric field. Besides, the debris observed has a diameter of 50–200 nm, possibly formed by heavier aggregates of the ions.<sup>20</sup> Therefore, the gravity influence on the movement of the aggregated ions should also be considered, which is very similar to the precipitation of gold nanoparticles in solution.<sup>21</sup> Considering the etching site's local environment in LaCBD, the deposition of etched materials can result from the combined influence of generation, diffusion, drifting, and gravity (Figure 3a). For simplicity, the following equations can be used to qualitatively describe the ions' deposition rate on the top and bottom sides:

$$\text{DR}_{\text{top}} = g(P) - D \frac{\partial n_{\text{top}}}{\partial r} + \mu \vec{E} n_{\text{top}} + n_{\text{top}} \frac{mg}{\xi} \quad (1)$$

$$\text{DR}_{\text{bottom}} = g(P) - D \frac{\partial n_{\text{bottom}}}{\partial r} - \mu \vec{E} n_{\text{bottom}} - n_{\text{bottom}} \frac{mg}{\xi} \quad (2)$$

DR is the deposition rate of silicic acid ions.  $g(P)$  is the generation rate of ions, which positively correlates with the laser power  $P$ .<sup>9</sup> Although the generation rate also positively correlates with chloride ions strength, the KCl concentration is fixed at 1 M for simplicity.<sup>8</sup>  $D$  is the diffusivity of ions.  $\mu$  is the electrophoretic mobility of ions.  $\vec{E}$  is the electric field, and  $n_{\text{top}}$  and  $n_{\text{bottom}}$  is the number of ions near the top and bottom surfaces. Due to the influence of gravity and electric field,  $n_{\text{top}}$  should be larger than  $n_{\text{bottom}}$ .  $m$  is the mass of ion aggregates,  $g$  is the acceleration of gravity, and  $\xi$  is the viscous drag on the ion aggregates given by Stokes' law.<sup>22</sup> Based on the deposition rate equations, the combined effect of diffusion, drifting, and

gravity can induce more silicic acid ion aggregates deposited on the top surface, as shown in Figure 3a. As previously discussed, the PL mapping on the bottom surface can indicate the amount of excess debris on both sides with a higher signal-to-noise ratio. Thus, the bottom-side PL is used to characterize the debris and the PL intensity at the debris accumulation region can be described as  $\text{PL} = \alpha R_s (\text{DR}_{\text{top}} + \text{DR}_{\text{bottom}})T$ , using eqs 1 and 2, yielding

$$\text{PL} = \alpha R_s \left[ 2g(P) - D \left( \frac{\partial n_{\text{top}}}{\partial r} + \frac{\partial n_{\text{bottom}}}{\partial r} \right) + \mu \vec{E} (n_{\text{top}} - n_{\text{bottom}}) + (n_{\text{top}} - n_{\text{bottom}}) \frac{mg}{\xi} \right] T \quad (3)$$

in which  $\alpha$  is the absorption coefficient,  $R_s$  is the surface roughness, and  $T$  is the etching time.

To validate the model with experiments, we studied the debris accumulation profile at various etching conditions through bottom-side PL mapping due to its in situ capability. First, we studied the etching cases without the electric field. Previous studies have suggested that increasing the laser power can accelerate the etching of SiN<sub>x</sub>, resulting in a higher generation rate ( $g(P)$ ) of the etched material.<sup>8,9</sup> Therefore, within the same etching time, the PL increment will be higher if a higher power laser is applied (eq 3). In the experiment, we applied 10, 40, and 60 mW lasers for 60 min on each sample. The real-time PL traces in Figure 3b show how PL intensity evolves during etching. The PL trace first decreased due to the decomposition of materials and then increased due to the accumulated debris around the etching spot. After 60 min of etching, the end-point PL maps of etching sites are collected, as shown in Figure 3c. It is clear that when a 60 mW laser is

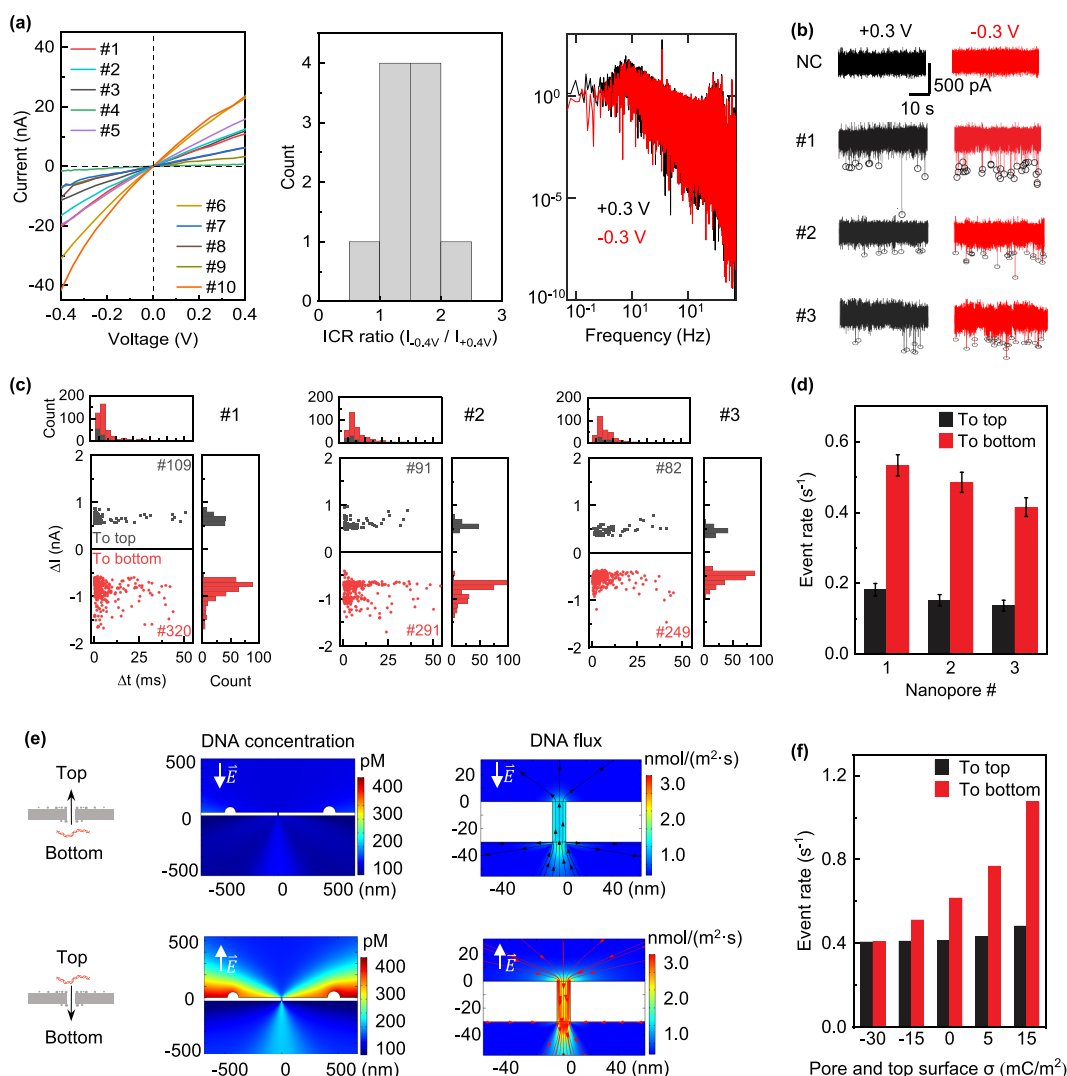


**Figure 4.** (a) The IV curves of 10 LaCBD nanopores show rectification. The histogram shows the distribution of the rectification ratio. Power density spectrum characterization of the LaCBD nanopore. (b) Negative control trace (using nanopore no. 1) and DNA translocation trace from three nanopores (no. 1, no. 2, and no. 3). 100 pM of 1 kbp dsDNA was filled on both sides. (c) The scatter plots of blockade current ( $\Delta I$ ) versus dwell time ( $\Delta t$ ). Plots were obtained from three nanopores, each measured for 10 min. (d) The bi-directional DNA translocation event rate of three different pores, black columns represent the bottom-to-top direction, and red columns represent the top-to-bottom direction. The error bars represent the Poisson counting uncertainty  $n^{1/2}/T$ . (e) The simulated DNA concentration and flux map under positive and negative voltages (+0.3 and -0.3 V). The streamlines show DNA's flux path. (f) Simulation shows the dependence of DNA event rate on pore and top surface charge density. The event rate is calculated by integrating DNA flux over the pore area. The bottom surface charge is fixed at  $-30 \text{ mC/m}^2$ .

applied, the mean PL inside the dashed circle is increased around the pore region compared with 20 and 40 mW, indicating more accumulated debris around the etching spot. These results suggest that PL increment is laser power-dependent. Second, we studied electric field strength's influence on PL increment. The laser power is fixed at 20 mW, and different positive voltages are applied during the etching. Based on our hypothesis, the etched material is the positively charged silicic acid ions. As a result, the higher electric field will increase ions' drifting speed, and the estimated PL using eq 3 will thus increase with higher voltage. In the experiment, 0, +0.5, and +1.0 V were applied at each etching spot for 5 min unless a pore formed. The real-time PL traces in Figure 3d showed a faster PL increment when a higher voltage was applied. After etching, the PL maps of each spot (Figure 3e) indicate more debris accumulated around the etching spot with increased voltage. The results suggest that

the etched material is positively charged, and the PL increment is voltage amplitude-dependent. In Figure S4, another sample shows a similar PL trend at varied voltages, and the formed debris cannot be rinsed away by IPA and distilled water since PL remains increased. Third, we also studied the influence of the electric field direction. While laser power is fixed at 20 mW, a voltage of either +6 or -6 V was applied in the experiment. When a negative voltage is applied, the drifting component  $\mu \vec{E}(n_{\text{top}} - n_{\text{bottom}})$  in eq 3 will negatively contribute to the PL intensity since the population-dominated top-side ions will drift away from the surface. In Figure 3f, the real-time PL trace of -6 V continuously decreases while the +6 V trace increases within 60 min of etching. The PL maps in Figure 3g further verified no noticeable debris accumulation for the -6 V case, and massive debris accumulated around the etching spot for the +6 V case. The result suggests that PL increment is electric field direction-dependent.

Overall, debris formation around the LaCBD nanopore results from the competition between material decomposition and deposition during the fabrication. Our model hypothesizes that the debris-induced PL increment depends on laser power, voltage amplitude, and electric field direction. In other words, the debris formation depends on the generation rate, drifting speed, and direction of positively charged ions. With higher laser power and a stronger electric field, debris formation will be faster. Besides, the debris formation can be alleviated by applying negative voltage on the top side.

**2.4. Impact of Asymmetrical Debris and Polarized Surface Charge on DNA Transport.** With a clearer image of debris formation in the LaCBD process, the impact of debris formation on nanopore sensing applications can be better understood. When characterizing the fabricated LaCBD nanopores, we found that most IV curves are rectified (Figure 4a) with a higher current amplitude at negative voltage bias. Meanwhile, the bi-directional DNA transport shows a preferable direction from top to bottom: DNA has a more frequent translocation from top to bottom than the other direction (Figure 4b,c). The scatter plots of DNA translocation events in Figure 4c show an identical pattern since detecting same-length DNA with three nanopores of similar size (10.83 nm for pore no. 1; 9.94 nm for pore no. 2; 8.88 nm for pore no. 3). The nanopore diameters are estimated by  $G = \sigma(4h/\pi D^2 + 1/D)^{-1}$ , in which  $\sigma$ ,  $h$ , and  $D$  represent the electrolyte conductivity, membrane thickness, and nanopore diameter, respectively.<sup>23</sup> Interestingly, the asymmetrical event rate phenomenon is observed in three different LaCBD nanopores (Figure 4d). The event rate of top-to-bottom translocation is around 200% higher than in the other direction. The previous study credits the unequal translocation rate to asymmetric nanopore geometry,<sup>8</sup> which is yet to be verified. Previous studies show that the current rectification and uneven molecular transport are usually observed in glass and polyethylene terephthalate (PET) nanopores due to their high aspect ratio instead of thin membrane-based nanopores.<sup>24–27</sup> With the direct evidence of debris around the nanopore and the proposed debris formation mechanism, the cause of asymmetric transport can be studied by simulating the molecular transport based on the actual morphology.

The SEM images in Figure 2d,e provide the actual morphology around the nanopore. A line is drawn through the center of the debris to collect the morphology profile (Figure S5a). ImageJ is then used to plot the line profile in gray values (Figure S5b), and the peak width can estimate the debris diameter. For simplicity, the debris particles are regarded as semispheres. Since the bottom surface barely shows accumulated debris, it was regarded as a flat surface without debris. With the extracted parameters from the SEM image, the whole nanopore system's geometry is built, as shown in Figure S5c. In the COMSOL simulation, a two-dimensional computational domain was used to study the effect of debris and surface charge on molecular and ionic transport. The details of boundary conditions are described in Figure S5d. As shown in Figure 3a, most of the positively charged ions travel away from the bottom surface. In the simulation, the surface charge density at the bottom surface was thus hypothesized to be the same as the intact SiN<sub>x</sub> membrane. The previous study shows that the surface charge density of the intact SiN<sub>x</sub> membrane is around  $-30 \text{ mC/m}^2$  at pH 8.<sup>28,29</sup> The charge density of the bottom surface is therefore set as  $-30 \text{ mC/m}^2$  to yield a realistic value. Due to

the deposition of positively charged ions, the top surface is most likely positively charged. Although the exact value of the top surface charge density cannot be determined, it can be hypothesized to be a value comparable to the bottom surface. The charge density of the top surface is thus set as  $+15 \text{ mC/m}^2$ . When a nanopore is formed, the positively charged ions at the top etching region can travel inside the nanopore via diffusion and electrophoresis. In this process, some of those ions can be deposited on the inner wall of the nanopore. Thus, the pore inner wall surface is also hypothesized to be positively charged with a value of  $+15 \text{ mC/m}^2$ .

In the simulation, both reservoirs are filled with 100 pM dsDNA. However, the simulation results showed that the DNA concentration around the pore has a noticeable difference when applying +0.3 V (DNA travels from bottom to top) or  $-0.3 \text{ V}$  (DNA travels from top to bottom). At +0.3 V, the DNA concentration reaches up to 150 pM, whereas at  $-0.3 \text{ V}$ , it reaches 400 pM (Figure 4e). This asymmetric DNA concentration profile can originate from two factors. First, the polarized surface charge profile will cause an uneven DNA distribution between two surfaces. While the electrostatic attraction enhances the concentration of negatively charged DNA at the top surface, the electrostatic repulsion reduces the DNA concentration at the bottom surface. Second, the asymmetry is further enlarged when applying voltage bias across the nanopore since the electroosmotic flow (EOF) will be in effect. When the electric field is applied across the LaCBD nanopore, a body force, called EOF, will act on the flow in the electrical double layer (EDL). In the molecular dynamics model, the EOF direction is determined by the surface charge polarity and electrical field direction and the velocity of the EOF is highly dependent on the surface charge density and size of the channel.<sup>30,31</sup> Besides, molecular transport is more dominated by EOF than electrophoresis (EP) when a smaller nanopore is used.<sup>32</sup> In our simulation (Figure S6a), the transport of DNA is dominated by EOF instead of EP due to the small pore size (10 nm) and relatively high surface charge density in the pore ( $+15 \text{ mC/m}^2$ ). In Figure 4e, when applying +0.3 V, most of the DNA flux will go through the pore while the DNA near the bottom surface will be driven away from the nanopore entrance due to the EOF. In comparison, the EOF on the top surface drives DNA toward the nanopore entrance when applying  $-0.3 \text{ V}$  (Figure 4e). The fluid motion caused by EOF further enriches the pore-region DNA at the top surface and depletes it at the bottom. Accordingly, the asymmetry of DNA concentration is further escalated by the EOF. The DNA flux density was integrated over the nanopore area to obtain the simulated DNA transport event rate.

To examine the impact of surface charge polarization on DNA translocation, we varied the surface charge density of the pore and top surface from  $-30$  to  $+15 \text{ mC/m}^2$  while maintaining the bottom surface charge density constant at  $-30 \text{ mC/m}^2$ . Figure 4f shows the relationship between surface charge density and event rate, indicating that the rectification ratio in DNA bi-directional transport increases as surface charge polarization rises. When there is no polarization (all pore, top, and bottom surface charges are  $-30 \text{ mC/m}^2$ ), the bare rectification demonstrates that debris-induced morphology change cannot impact DNA transport behavior. Hence, the surface charge polarization primarily induces the DNA transport behavior. In Figure 4f, the top-to-bottom event rate is approximately 130% higher than in the other direction when



the pore and top surface charge is  $+15 \text{ mC/m}^2$ . As discussed, the higher DNA concentration at the top surface when applying negative bias can be the primary reason for this rectified molecular transport (no discernible difference in fluid velocity inside the pore at negative/positive voltage bias, as shown in Figure S6b). Although this simulated rectification ratio is smaller than the experimental result ( $\sim 200\%$ , Figure 4e), the overall DNA transport showed the same preferable direction from top to bottom, proving the polarized surface charge hypothesis.

Regarding the ionic transport, no prominent current rectification is found in the simulation compared with the experimental result (Figure S6c, Figure 4a). Several reasons can cause the simulation's low current rectification ratio (1.075). First, the hypothesized surface charge density can be underestimated and strongly affect the EOF velocity and ionic transport. Increasing the charge density can strengthen the polarization between the top and bottom surfaces, leading to a higher rectification ratio. The previous study shows that the asymmetric surface distribution can lead to the IV rectification at a low salt concentration (10 mM) even though the nanopore geometry is symmetric.<sup>33</sup> Second, the pore shape used in the simulation is hypothesized to be cylindrical, which eliminates the effect of asymmetrical pore geometry.<sup>24,25</sup> In LaCBD, the nanopores have been formed with dielectric breakdown. Their actual geometry and surface charge densities cannot readily be determined. The current will be rectified if the nanopore has a conical shape due to the ion accumulation and depletion inside the nanopore.<sup>24</sup> In a high aspect-ratio conical nanopore, the transfer of molecules will also have a preferred direction over another.<sup>25</sup> Therefore, the asymmetrical geometry of the nanopores can also induce rectification in ionic and molecular transport. However, the 30 nm  $\text{SiN}_x$  membrane used in the experiments will not likely form a high aspect-ratio conical nanopore.

Overall, the observed rectification in DNA transport is most likely attributed to the deposition of positively charged debris on the top surface and pore. This polarized surface charge distribution around the pore results in an asymmetrical DNA concentration between surfaces, and the EOF enhances the rectification in molecular transport. The similarity between measurement and simulation shows that rectified molecular transport can result from the increased DNA concentration at the top-side pore entrance due to debris-induced polarized surface charges. In summary, the alteration in morphology due to debris may not impact DNA transport behavior. However, the surface charge polarization induced by debris appears to be the leading cause of rectified DNA transport in LaCBD nanopores.

### 3. CONCLUSIONS

In this study, we reported on the formation of debris around the nanopore region in LaCBD due to the laser, a unique phenomenon not observed in the conventional CBD method. The SEM and PL spectroscopy characterization confirmed the presence of debris, which exhibited asymmetric distribution on the top and bottom sides of the membrane. An unexpected rectified ionic and molecular transport was also observed in those LaCBD nanopores with debris. Based on these observations, we developed a model describing the debris formation kinetics in LaCBD by considering the generation, diffusion, drift, and gravity in viscous mediums. The model hypothesized that the etched materials can be positively

charged and accumulate at the pore region, which would be affected by the laser power and electrical field. Experimental results validated the model and suggested that higher laser power or voltage stress would escalate debris formation in LaCBD by enhancing debris generation and drift. Conversely, a negative bias on the top side reduced debris formation since the etched material drifted away from the membrane. Additional simulations indicate that the rectification observed in molecular transport may be primarily attributed to the surface charge polarization around the pore rather than changes in morphology caused by the debris. These findings suggest that while the laser helps localize nanopores in LaCBD, caution should be taken due to the possibility of debris formation and rectification of molecular transport. We believe this study would provide valuable insights into the kinetics of LaCBD and the characteristics of the LaCBD nanopore.

### 4. METHODS

**4.1. Materials and Chemicals.**  $\text{SiN}_x$  membranes of 12 and 30 nm thickness were used in our experiments (Norcada, Canada). The square membrane with a  $50 \times 50 \mu\text{m}^2$  window is at the center of a  $200 \mu\text{m}$ -thick silicon frame. The  $\text{SiN}_x$  membranes were mounted into a PMMA-based flow cell with Ecoflex-5 (Smooth-On, USA). Ag/AgCl electrodes were house made with 0.375 mm Ag wires (Warner Instruments, USA). Potassium chloride (KCl) and 1× EDTA Tris buffer solution (pH 8.0, 10 mM Tris-HCl, 1 mM disodium EDTA) were purchased from Sigma-Aldrich. The 1 M KCl solution was made and filtered with a  $0.2 \mu\text{m}$  Anotop filter (Whatman, UK) and degassed in a vacuum chamber before use. A 1 kbp dsDNA fragment (Thermo Scientific, USA) was used for the nanopore experiment.

**4.1.1. LaCBD Experimental Setup and Laser Focusing.** The  $\text{SiN}_x$  membrane was mounted into a flow cell with a transparent quartz coverslip bottom that allowed laser access. The top and bottom chambers were filled with 1 M KCl in 1× EDTA Tris buffer. The flow cell was mounted on a nano-positioner (Physik Instrumente, P-611.3S NanoCube). The Keithley 2636 was used to apply voltage bias and collect current signals through Ag/AgCl electrodes. For LaCBD nanopore fabrication, the 488 nm laser is chosen due to its much faster etching rate compared with 532 and 645 nm lasers.<sup>13</sup> The 488 nm laser (Coherent OBIS 488 LS) was expanded to fill the back aperture before focusing at the  $\text{SiN}_x$  membrane through the objective lens (magnification 40×, numerical aperture 0.75) to form a diffraction-limited spot for confocal illumination. The laser spot radius is around  $1.2 \mu\text{m}$ . The emitted light was collected by the same objective lens and focused on a pinhole with a  $25 \mu\text{m}$  diameter (1–25 + B-1 + M-0.5, National Aperture) for improved spatial resolution. The emitted light passed through a bandpass filter before detection by the single photon counting module (SPCM-AQRH-13). A neutral-density (ND) filter was mounted in the front of the photon counter to expand the dynamic range. A CMOS camera (DCC1545M, Thorlabs) was also equipped to monitor the microscopic changes and acquire pixel intensities. A Faraday cage shielded the whole setup to minimize electromagnetic interference.

The CMOS camera and nano-positioner were used to focus the laser. The CMOS camera can capture 8-bit grayscale images, and the pixel intensity ranges from 0 to 255. The exposure time will be adjusted to avoid intensity saturation. First, the laser is coarsely focused by manually adjusting the sample's  $z$  position until the laser spot is the smallest. Second, when imaging with the CMOS camera, the pixel with the highest intensity will be regarded as the laser spot center. The average intensity of the center pixel and the surrounding 4 pixels will be used for focusing. Third, a customized LabView program will move the sample with a 100 nm step in the  $10 \mu\text{m}$  range and collect pixel intensity simultaneously to find the position of the maximum intensity. Fourth, the program will focus finely with a 5 nm step in the  $4 \mu\text{m}$  range. Finally, the sample will be automatically moved to the  $Z$  position of the maximum pixel intensity.

**4.1.2. In Situ Simultaneous PL and IC Characterization.** The SiN<sub>x</sub> membrane was assembled in a flow cell and mounted on the nanopositioner. The membrane was imaged using a CMOS camera to obtain a bright-field view and capture pixel intensity. A 488 nm Gaussian profile laser beam was used for LaCBD. A single-photon counting module (SPCM) was used for the PL characterization of the SiN<sub>x</sub> membrane. A pair of Ag/AgCl electrodes across the membrane was used to apply a voltage for the dielectric breakdown and IC mapping. This setup enabled us to perform the LaCBD,<sup>9</sup> scanning PL for material characterization, and laser-enhanced IC mapping<sup>6</sup> for nanopore location in a single platform. The 1 mW laser and 0.1 V voltage stress were used for the PL and IC mapping. After obtaining the bottom-side PL map, the SiN<sub>x</sub> membrane was flipped and remounted. Then, the top side was scanned with the laser to get the PL map. The normalized PL (NPL) heat map was obtained by normalizing the original PL heat map with the PL intensity of the SiN<sub>x</sub> region that was not etched.

**4.1.3. Nanopore Sensing and Data Analysis.** Ag/AgCl electrodes were placed at each side of the SiN<sub>x</sub> membrane. The conductance of the nanopore was determined by performing a linear fit of the IV curve within the range of −400 to 400 mV. When detecting DNA, both top and bottom reservoirs were filled with 100 pM 1 kbp dsDNA (in 1 M KCl) and a typical voltage of 300 mV was applied across the pore by 6363 DAQ card (National Instruments, USA). A trans-impedance amplifier (Axopatch 200B, Molecular Devices, USA) was used to amplify the resulting current and then digitized by the 6363 DAQ card at a 100 kHz sampling rate. Finally, a customized MATLAB (MathWorks) software was used to analyze the current time trace and extract the DNA translocation information. The threshold of the event peak was set at six times of standard deviation of the current traces. If clogging was observed, five times IV sweeps from −600 to 600 mV were applied to restore the pore.

**4.2. SEM Imaging of the SiN<sub>x</sub> Membrane.** To prepare the membrane sample for SEM characterization, both sides of the SiN<sub>x</sub> membrane were coated with 10 nm-thick iridium through a sputter coating process. The membrane was characterized by scanning electron microscopy (Verios, Thermo Scientific, USA). The accelerating voltage is 3.0 kV, the current is 0.1 nA, and the working distance is 3.0 mm.

**4.3. Simulation.** COMSOL Multiphysics 5.4 was used for the nanopore simulation. The details of geometry parameters and boundary conditions are described in Figure S5 and Table S1.

## ■ ASSOCIATED CONTENT

### SI Supporting Information

The Supporting Information is available free of charge at <https://pubs.acs.org/doi/10.1021/acsami.3c03123>.

Detailed descriptions of auto-focusing, current traces for breakdown, additional samples' PL and SEM characterization, PL characterization of a 12 nm-thick SiN<sub>x</sub> membrane, another sample showing the correlation between voltage stress and PL increment, DNA bi-directional transport current traces, COMSOL simulation settings and results, and a table of the parameters used in the numerical simulation (PDF)

## ■ AUTHOR INFORMATION

### Corresponding Author

Weihua Guan — Department of Electrical Engineering and Department of Biomedical Engineering, Pennsylvania State University, University Park, Pennsylvania 16802, United States; [orcid.org/0000-0002-8435-9672](https://orcid.org/0000-0002-8435-9672); Email: [wzg111@psu.edu](mailto:wzg111@psu.edu)

## Authors

Ming Dong — Department of Electrical Engineering, Pennsylvania State University, University Park, Pennsylvania 16802, United States; [orcid.org/0000-0002-9071-5717](https://orcid.org/0000-0002-9071-5717)

Reza Nouri — Department of Electrical Engineering, Pennsylvania State University, University Park, Pennsylvania 16802, United States

Zifan Tang — Department of Electrical Engineering, Pennsylvania State University, University Park, Pennsylvania 16802, United States

Complete contact information is available at: <https://pubs.acs.org/doi/10.1021/acsami.3c03123>

## Author Contributions

W.G. conceived the concept and supervised the study. M.D. performed LaCBD nanopore experiments. Z.T. helped build the setup, and R.N. helped develop the COMSOL simulation. W.G. and M.D. co-wrote the manuscript and discussed it with all other authors.

## Notes

The authors declare no competing financial interest.

## ■ ACKNOWLEDGMENTS

This work was partially supported by the National Science Foundation under Grant No. ECCS-2045169. Any opinions, findings, and conclusions or recommendations expressed in this work are those of the authors and do not necessarily reflect the views of the National Science Foundation.

## ■ REFERENCES

- (1) Kim, M. J.; Wanunu, M.; Bell, D. C.; Meller, A. Rapid Fabrication of Uniformly Sized Nanopores and Nanopore Arrays for Parallel DNA Analysis. *Adv. Mater.* **2006**, *18*, 3149–3153.
- (2) Wu, M.-Y.; Smeets, R. M.; Zandbergen, M.; Ziese, U.; Krapf, D.; Batson, P. E.; Dekker, N. H.; Dekker, C.; Zandbergen, H. W. Control of Shape and Material Composition of Solid-State Nanopores. *Nano Lett.* **2009**, *9*, 479–484.
- (3) Kwok, H.; Briggs, K.; Tabard-Cossa, V. Nanopore Fabrication by Controlled Dielectric Breakdown. *PLoS One* **2014**, *9*, No. e92880.
- (4) Waugh, M.; Briggs, K.; Gunn, D.; Gibeault, M.; King, S.; Ingram, Q.; Jimenez, A. M.; Berryman, S.; Lomovtsev, D.; Andrzejewski, L.; Tabard-Cossa, V. Solid-State Nanopore Fabrication by Automated Controlled Breakdown. *Nat. Protoc.* **2020**, *15*, 122–143.
- (5) Yemini, M.; Hadad, B.; Liebes, Y.; Goldner, A.; Ashkenasy, N. The Controlled Fabrication of Nanopores by Focused Electron-Beam-Induced Etching. *Nanotechnology* **2009**, *20*, 245302.
- (6) Dong, M.; Tang, Z.; He, X.; Guan, W. Direct Observation of Redox-Induced Bubble Generation and Nanopore Formation Dynamics in Controlled Dielectric Breakdown. *ACS Appl. Electron. Mater.* **2020**, *2*, 2954–2960.
- (7) Ying, C.; Houghtaling, J.; Eggenberger, O. M.; Guha, A.; Nirmalraj, P.; Awasthi, S.; Tian, J.; Mayer, M. Formation of Single Nanopores with Diameters of 20–50 nm in Silicon Nitride Membranes Using Laser-Assisted Controlled Breakdown. *ACS Nano* **2018**, *12*, 11458–11470.
- (8) Yamazaki, H.; Hu, R.; Zhao, Q.; Wanunu, M. Photothermally Assisted Thinning of Silicon Nitride Membranes for Ultrathin Asymmetric Nanopores. *ACS Nano* **2018**, *12*, 12472–12481.
- (9) Tang, Z.; Dong, M.; He, X.; Guan, W. On Stochastic Reduction in Laser-Assisted Dielectric Breakdown for Programmable Nanopore Fabrication. *ACS Appl. Mater. Interfaces* **2021**, *13*, 13383–13391.
- (10) Gilboa, T.; Zvuloni, E.; Zrehen, A.; Squires, A. H.; Meller, A. Automated, Ultra-Fast Laser-Drilling of Nanometer Scale Pores and Nanopore Arrays in Aqueous Solutions. *Adv. Funct. Mater.* **2020**, *30*, 1900642.



- (11) Datta, M.; Romankiw, L.; Vigliotti, D.; Von Gutfeld, R. Laser Etching of Metals in Neutral Salt Solutions. *Appl. Phys. Lett.* **1987**, *51*, 2040–2042.
- (12) Chung, C.-K.; Lin, Y.-C.; Huang, G. Bulge Formation and Improvement of the Polymer in Co<sub>2</sub> Laser Micromachining. *J. Micromech. Microeng.* **2005**, *15*, 1878.
- (13) Gilboa, T.; Zrehen, A.; Girsault, A.; Meller, A. Optically-Monitored Nanopore Fabrication Using a Focused Laser Beam. *Sci. Rep.* **2018**, *8*, 1–10.
- (14) He, X.; Tang, Z.; Liang, S.; Liu, M.; Guan, W. Confocal Scanning Photoluminescence for Mapping Electron and Photon Beam-Induced Microscopic Changes in Sinx During Nanopore Fabrication. *Nanotechnology* **2020**, *31*, 395202.
- (15) Luna-López, J.; Morales-Sánchez, A.; Aceves-Mijares, M.; Yu, Z.; Domínguez, C. Analysis of Surface Roughness and Its Relationship with Photoluminescence Properties of Silicon-Rich Oxide Films. *J. Vac. Sci. Technol., A* **2009**, *27*, 57–62.
- (16) Zvuloni, E.; Zrehen, A.; Gilboa, T.; Meller, A. Fast and Deterministic Fabrication of Sub-5 Nanometer Solid-State Pores by Feedback-Controlled Laser Processing. *ACS Nano* **2021**, *15*, 12189–12200.
- (17) Filippov, S.; Jansson, M.; Stehr, J. E.; Palisaitis, J.; Persson, P. Å.; Ishikawa, F.; Chen, W. M.; Buyanova, I. A. Strongly Polarized Quantum-Dot-Like Light Emitters Embedded in GaAs/GaN Core/Shell Nanowires. *Nanoscale* **2016**, *8*, 15939–15947.
- (18) Yanagi, I.; Akahori, R.; Hatano, T.; Takeda, K. I. Fabricating Nanopores with Diameters of Sub-1 Nm to 3 Nm Using Multilevel Pulse-Voltage Injection. *Sci. Rep.* **2014**, *4*, 1–7.
- (19) Schaefer, J.; Backus, E. H.; Bonn, M. Evidence for Auto-Catalytic Mineral Dissolution from Surface-Specific Vibrational Spectroscopy. *Nat. Commun.* **2018**, *9*, 1–6.
- (20) Choi, J.-H.; Choi, H. R.; Jeon, J.; Cho, M. Ion Aggregation in High Salt Solutions. VII. The Effect of Cations on the Structures of Ion Aggregates and Water Hydrogen-Bonding Network. *J. Chem. Phys.* **2017**, *147*, 154107.
- (21) Powell, J.; Schwieters, R.; Bayliff, K.; Herman, E.; Hotvedt, N.; Changstrom, J.; Chakrabarti, A.; Sorensen, C. Temperature Dependence of Solubility of Gold Nanoparticle Suspension/Solutions. *RSC Adv.* **2016**, *6*, 70638–70643.
- (22) Pau, P. C. F.; Berg, J.; McMillan, W. Application of Stokes' Law to Ions in Aqueous Solution. *J. Phys. Chem.* **1990**, *94*, 2671–2679.
- (23) Kowalczyk, S. W.; Grosberg, A. Y.; Rabin, Y.; Dekker, C. Modeling the Conductance and DNA Blockade of Solid-State Nanopores. *Nanotechnology* **2011**, *22*, 315101.
- (24) Tseng, S.; Lin, S.-C.; Lin, C.-Y.; Hsu, J.-P. Influences of Cone Angle and Surface Charge Density on the Ion Current Rectification Behavior of a Conical Nanopore. *J. Phys. Chem. C* **2016**, *120*, 25620–25627.
- (25) Chen, K.; Bell, N. A.; Kong, J.; Tian, Y.; Keyser, U. F. Direction- and Salt-Dependent Ionic Current Signatures for DNA Sensing with Asymmetric Nanopores. *Biophys. J.* **2017**, *112*, 674–682.
- (26) Kovarik, M. L.; Zhou, K.; Jacobson, S. C. Effect of Conical Nanopore Diameter on Ion Current Rectification. *J. Phys. Chem. B* **2009**, *113*, 15960–15966.
- (27) Sexton, L. T.; Horne, L. P.; Martin, C. R. Developing Synthetic Conical Nanopores for Biosensing Applications. *Mol. BioSyst.* **2007**, *3*, 667–685.
- (28) Buyukdagli, S.; Ala-Nissila, T. Ph-Mediated Regulation of Polymer Transport through Sin Pores. *Europhys. Lett.* **2018**, *123*, 38003.
- (29) Lin, C.-Y.; Turker Acar, E.; Polster, J. W.; Lin, K.; Hsu, J.-P.; Siwy, Z. S. Modulation of Charge Density and Charge Polarity of Nanopore Wall by Salt Gradient and Voltage. *ACS Nano* **2019**, *13*, 9868–9879.
- (30) Rezaei, M.; Azimian, A.; Semiromi, D. T. The Surface Charge Density Effect on the Electro-Osmotic Flow in a Nanochannel: A Molecular Dynamics Study. *Heat Mass Transfer* **2015**, *51*, 661–670.
- (31) Ghosal, S.; Sherwood, J. D.; Chang, H.-C. Solid-State Nanopore Hydrodynamics and Transport. *Biomicrofluidics* **2019**, *13*, No. 011301.
- (32) Zhang, Y.; Zhao, J.; Si, W.; Kan, Y.; Xu, Z.; Sha, J.; Chen, Y. Electroosmotic Facilitated Protein Capture and Transport through Solid-State Nanopores with Diameter Larger Than Length. *Small Methods* **2020**, *4*, 1900893.
- (33) Van Oeffelen, L.; Van Roy, W.; Idrissi, H.; Charlier, D.; Lagae, L.; Borghs, G. Ion Current Rectification, Limiting and Overlimiting Conductances in Nanopores. *PLoS One* **2015**, *10*, No. e0124171.

## Recommended by ACS

### Plasmonic Bowl-Shaped Nanopore for Raman Detection of Single DNA Molecules in Flow-Through

Yingqi Zhao, Francesco De Angelis, *et al.*

JUNE 01, 2023  
NANO LETTERS

READ 

### Discrimination of Short ssDNA Using Nanopore-Fabricated Self-Assembled Metal–Organic Framework Membranes

Libo Zhu, Renjun Pei, *et al.*

DECEMBER 06, 2022  
ACS APPLIED NANO MATERIALS

READ 

### Toehold-Mediated Shape Transition of Nucleic Acid Nanoparticles

Jordan Hartung, Emil F. Khisamutdinov, *et al.*

MAY 19, 2023  
ACS APPLIED MATERIALS & INTERFACES

READ 

### Computer-Aided Design of A-Trail Routed Wireframe DNA Nanostructures with Square Lattice Edges

Marco Lolaico, Björn Högberg, *et al.*

MARCH 23, 2023  
ACS NANO

READ 

Get More Suggestions >